Electronic spectroscopy of ytterbium in a neon matrix

R. Lambo, A. A. Buchachenko, L. Wu, Y. Tan, J. Wang et al.

Citation: J. Chem. Phys. **137**, 204315 (2012); doi: 10.1063/1.4768419
View online: http://dx.doi.org/10.1063/1.4768419
View Table of Contents: http://jcp.aip.org/resource/1/JCPSA6/v137/i20
Published by the American Institute of Physics.

Electronic spectroscopy of ytterbium in a neon matrix

R. Lambo,[1,a)] A. A. Buchachenko,[2] L. Wu,[1] Y. Tan,[1] J. Wang,[1] Y. R. Sun,[1] A.-W. Liu,[1] and S.-M. Hu[1]

[1]*Hefei National Laboratory for Physical Science at the Microscale, University of Science and Technology of China, Hefei, Anhui 230026, China*

[2]*Department of Chemistry, M. V. Lomonosov Moscow State University, Moscow 119991, Russia*

(Received 25 August 2012; accepted 6 November 2012; published online 30 November 2012)

The low-lying electronic states of Yb isolated in a solid Ne matrix are characterized through absorption and emission spectroscopy. The absorption spectra of matrix isolated Yb while pumped into its triplet states have been recorded for the first time and the 6s6p $^3P_J \rightarrow$ 5d6s $^3D_{1,2}$ transition frequencies obtained. Under matrix conditions, the structure of these states is found to be qualitatively the same as in the free atom, but the intersystem crossing rate is observed to be several orders of magnitude greater. A proposed explanation for this is curve crossings between the bound potential energy surface correlated to the 6s6p $^1P_1$ state and the potential energy surfaces correlated to the 5d6s $^3D_{1,2}$ states in isolation. The potentials of the Yb · Ne dimer in its lowest electronic states are computed *ab initio* and used in a pairwise cluster model to explicitly demonstrate these curve crossings.
 [http://dx.doi.org/10.1063/1.4768419]

I. INTRODUCTION

As a lanthanide with an ns^2 S ground state, Yb is at the intersection of two groups of atoms that have proved remarkably fruitful in studies of metal atoms (M) embedded in solid rare gases (RGs). As exemplified by the extensive work done on Group 12 species,[1–3] spherically symmetric ns^2 S ground state atoms have long been favored because of their simple low-lying electronic structure, consisting of spin-singlet and -triplet states with allowed transitions amenable to UV-visible laser excitation. Furthermore, the wide availability of accurate M · RG interaction potentials for them allowed one to study the effects of matrix isolation using M · RG_n cluster models.[4–6] Meanwhile, the site-selected emission spectroscopy of the lanthanide europium has recently revealed such unique phenomena as its tendency to occupy two distinct thermally stable sites[7] and the formation of its cation through a multiphoton ionization process.[8]

Work on the lanthanides in matrix isolation has nonetheless been relatively limited, in part because of the absence of any M · RG interaction potentials for them. Indeed, Ho[9] and Yb[10] are the only other species for which spectra have been recorded in more than one rare gas. In the present work, we have made a further contribution to the study of Yb under matrix conditions by characterizing its low-lying electronic states (Figure 1) in solid Ne. In addition to standard absorption and emission spectroscopy, we have performed the absorption spectroscopy of Yb in its excited triplet states. As far as we have been able to determine, the detailed absorption spectra of a matrix isolated species in its excited states have only been reported once before, for Cr in solid Ar and Kr.[11]

Previous work on the Yb/Ne system focused mainly on emission from the triplet manifold[12] and demonstrated the unusually high efficiency of the singlet-to-triplet intersystem crossing (ISC). Here, by observing the 6s6p $^3P_J \rightarrow$ 5d6s $^3D_{1,2}$ transitions in isolation, we have concluded that a matrix-induced interaction between the $^3D_{1,2}$ states and the $^1P_1$ state is responsible. In support of this conjecture, we have generated the potential energy surfaces (PESs) of the Yb · Ne_{18} cluster using a pairwise potential model that accounts for the anisotropy of Yb · Ne interactions. The individual Yb · Ne potentials were obtained by *ab initio* spin-orbit calculations. These simulations identified curve crossings between the cluster PESs correlated to the $^3D_{1,2}$ and $^1P_1$ states as the dominant mechanism for enhanced ISC.

The organization of this paper is as follows: In Secs. II and III, the experimental methods and results are presented. In Sec. IV, we briefly formulate the pairwise potential model and present the results of the cluster model. Experimental and theoretical results are discussed together in Sec. V, and conclusions and perspectives summarized in Sec. VI.

II. EXPERIMENTAL

The experimental setup was similar to those used by our group in previous experiments[13] and so is only briefly described here. The principal apparatus for infrared absorption spectroscopy was a Fourier transform (FT) spectrometer (Bruker IFS120 HR). Light from a tungsten lamp passing through a CaF_2 beam splitter provided a white-light continuum for the registration of absorption spectra with a germanium detector. The spectral region selected for observation was from 5000 to 12 000 cm^{-1} with an unapodized resolution of 2 cm^{-1}.

The FT chamber was isolated from the sample chamber and evacuated to a pressure of 40 Pa to minimize absorptions due to air appearing in the spectra. We selected a 1 in. diameter BaF_2 window as the substrate on which to grow the matrix for its optical transparency in the infrared region. It was

a)Electronic mail: lambo@mail.ustc.edu.cn.

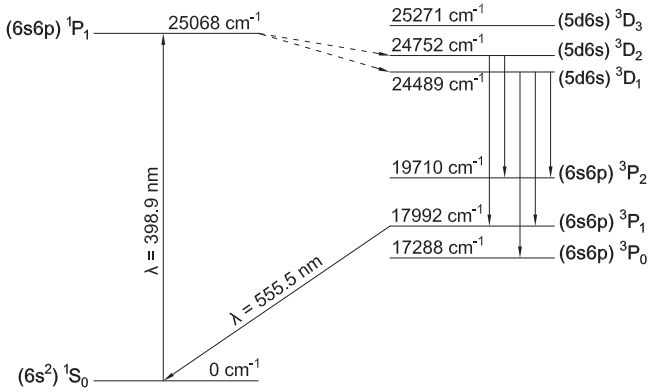

FIG. 1. Optical pumping scheme for low-lying electronic levels of Yb in the gas phase, showing allowed transitions and corresponding frequencies.

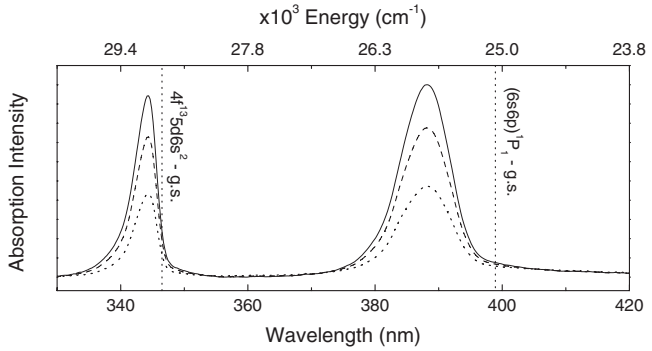

FIG. 2. White-light absorption spectra showing the peaks due to the $6s^2\ ^1S_0 \rightarrow 4f^{13}5d^26s$ and $6s^2\ ^1S_0 \rightarrow 6s6p\ ^1P_1$ transitions. The dashed trace shows the result of an annealing cycle in which the matrix was raised to 8 K for 10 min. The dotted trace shows the result of a second identical annealing cycle.

maintained at a temperature of 4.2 K by being thermally anchored to the coldhead of a closed-cycle helium refrigerator (Janis SHI-4-5) in the sample chamber, itself evacuated to a pressure of 10^{-5} Pa. The matrix was prepared by co-depositing a small Ne flux (∼99.99% pure provided by Nanjing Special Gas Inc.) together with a Yb atomic beam produced by a Knudsen effusion oven. Typical operating conditions were an oven temperature of approximately 390 °C and a flux of 0.5−1.0 SCCM maintained by a mass flow controller (MKS 1479A) for 2 h.

Two high power light-emitting diodes (LEDs) were used as optical pumps to transfer the Yb population into the 6s6p ^3P_J state: one centered at 385 nm and another centered at 405 nm. The LEDs have a bandwidth (∼5 nm) that is considerably broader than that of a laser, but have the advantage of being able to produce a light source with an intensity of 100 mW/cm^2. Once the matrix had been prepared, the focus of the LED was aligned to be coincident on its surface with the FT probe light that detected absorptions originating from the 6s6p ^3P_J state.

UV-visible spectroscopy was performed in a different sample chamber with more optical access than that of the Bruker, using a Thorlabs CCS 2000 spectrometer capable of a resolution of 0.5 nm. The gas handling system, oven, and closed-cycle refrigerator, however, remained the same. Continuous white-light absorption spectra were obtained using emission from a deuterium lamp passing directly through the matrix. Emission spectra were measured perpendicular to the matrix for which we had two optical pumps. The first was a Ti:Sapphire ring laser whose frequency was doubled to produce a narrow-band (∼1 MHz) 2 mW/cm^2 source at 389 nm. The second was an LED coupled to a monochromator (Zolix, model Omni-λ 300) with a 1200 groves/mm diffraction grating blazed at 300 nm. The slit width of the monochromator during the emission spectroscopy was 0.37 mm providing a resolution of 1 nm. We measured the lifetime of the 6s6p $^3P_0$ state using a PMT and selected the emission wavelength of interest using the same monochromator with a slit width of 1.85 mm corresponding to a 5 nm resolution.

The temperature of the system was monitored using a silicon diode sensor (DT-470) mounted on the baseplate holding the substrate and read off a temperature controller (Lake Shore 331S). A resistive heater mounted on the coldhead gave us the option of heating the substrate. However, we found the Yb sample to be easily lost under heating and so did not perform any systematic temperature studies.

III. RESULTS

A. Absorption spectra

The UV-visible absorption spectra of the Yb/Ne sample are shown in Figure 2. Two spectral features can be readily identified: one centered at 344 nm and another centered at 388 nm. The atomic transitions nearest in frequency to these absorption peaks are, respectively, the $6s^2\ ^1S_0 \rightarrow 4f^{13}5d6s^2$ and $6s^2\ ^1S_0 \rightarrow 6s6p\ ^1P_1$ transitions. The proximity of the absorption peaks to these lines means that we can confidently identify the corresponding transitions in the solid state. Our assignments, summarized in Table I, broadly agree with previously published results.[12]

Annealing cycles were performed by heating the sample to 8 K for 10 min and each annealing cycle was found to reduce the Yb population by approximately 25%. Within error, though, there appeared to be no change in the positions and linewidths of the absorption peaks, which indicates that there is negligible Yb occupation in thermally unstable trapping sites.

Results from the absorption spectra were used to calibrate our matrix growth conditions. Observation of interference fringes with a helium-neon laser operating at 635 nm during deposition gave the final matrix thickness to be 30 μm. Assuming that the gas phase oscillator strength of the $6s^2\ ^1S_0 \rightarrow 6s6p\ ^1P_1$ transition is unchanged in the solid state, we estimated our typical Yb:Ne dilution at 2.5×10^{-6}.

TABLE I. Principal features of the white-light absorption spectra of the Yb/Ne system. Here, λ and ν refer, respectively, to the wavelength and transition frequency; Δ refers to the transition linewidth (FWHM); δ refers to the matrix frequency shift relative to the gas phase transition frequency. An uncertainty of ±40 (cm^{-1}) is assumed on all values.

Transition	λ (nm)	ν (cm^{-1})	Δ (cm^{-1})	δ (cm^{-1})
$6s^2\ ^1S_0 \rightarrow 4f^{13}5d^26s$	344.1	29 060	320	190
$6s^2\ ^1S_0 \rightarrow 6s6p\ ^1P_1$	388.3	25 750	550	680

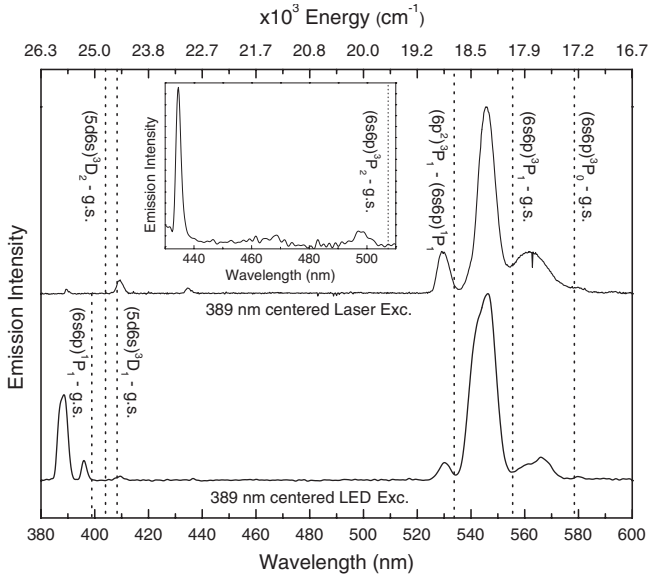

FIG. 3. Spectra produced by excitation from a laser (top) and an LED coupled to a monochromator (bottom). A longpass filter with a 400 nm cutoff was placed over the spectrometer during laser excitation to suppress scattering. In both layers, this scattering appears as a peak centered at 389 nm. The apparent structure at 563 nm (top) reflects a point defect in the CCD of the spectrometer.

B. Emission spectra

Emission spectra were recorded from an annealed sample using the Ti:Sapphire laser and the LEDs as optical pumps. Since LEDs were used to perform excited state absorption spectroscopy, we wished to demonstrate that they would be equally effective in populating the triplet states. Figure 3 compares the two spectra, the principal details of which are summarized in Table II.

In the spectral region close to that of the gas phase 6s6p ^3P_J manifold, three main emission peaks at 530 nm, 546 nm, and 562 nm were observed. The emission corresponding to the $^3P_0$ state was clearly identified through a lifetime measurement. In the gas phase, this state is metastable with a long lifetime, estimated theoretically to be 55.9 s.[14] The decay curve of the 562 nm emission was adequately fit by a single exponential with a time constant of 14.5 ± 0.5 s and therefore assigned to the 6s6p $^3P_0 \rightarrow 6s^2\ ^1S_0$ transition. The $^3P_2$ state is also metastable with a calculated lifetime of 12.3 s.[14] Lifetime measurements of the 546 nm and 530 nm emissions revealed that they decay faster than the 25 ms resolution available to us and so are unlikely to originate from the $^3P_2$ state.

The strong 546 nm emission can therefore be confidently assigned to the only allowed electric dipole transition, 6s6p $^3P_1 \rightarrow 6s^2\ ^1S_0$. Meanwhile, the gas phase transition closest in frequency to the 530 nm emission is the $6p^2\ ^3P_1 \rightarrow$ 6s6p $^1P_1$ decay at 533 nm. The peak minimally visible above the background noise at 498 nm (Figure 3 (inset)) was then assigned to the 6s6p $^3P_2 \rightarrow 6s^2\ ^1S_0$ transition. We found supporting evidence for these assignments in the excited state absorption spectra of Yb.

In the 400−440 nm region of the spectra, three emission peaks originating from the P- and D-states were observed. The peak centered at 396 nm was assigned to the 6s6p $^1P_1 \rightarrow 6s^2\ ^1S_0$ decay. Of the remaining two, the higher energy 410 nm peak was assigned to the 5d6s $^3D_2$ state decay, while the lower energy 435 nm peak was assigned to the 5d6s $^3D_1$ state decay.

We also note that the emission spectra of Figure 3 indicates that Yb occupies at least two distinct trapping sites that are thermally stable within the temperature range of the annealing cycle. With laser excitation, a weak blue feature starting at 540 nm and extending to 535 nm is visible in the large peak assigned to the 6s6p $^3P_1 \rightarrow 6s^2\ ^1S_0$ decay. With LED excitation, this peak is even more asymmetric, with a large blue shoulder appearing in the 535−550 nm region. A similar shoulder appears in the 555−562 nm region to the blue of the 6s6p $^3P_0 \rightarrow 6s^2\ ^1S_0$ emission peak. These observations are well explained by a larger proportion of a secondary Yb population being excited with the broadband LED.

TABLE II. Principal features of the emission spectrum for the Yb/Ne system produced by laser excitation. The symbols here are the same as those used in Table I. The uncertainty is assumed to be ±40 cm^{-1} on all values.

Transition	λ (nm)	ν (cm^{-1})	Δ (cm^{-1})	δ (cm^{-1})
6s6p $^1P_1 \rightarrow 6s^2\ ^1S_0$[a]	396.1	25 250	140	180
5d6s $^3D_2 \rightarrow 6s^2\ ^1S_0$	409.5	24 420	160	−330
5d6s $^3D_1 \rightarrow 6s^2\ ^1S_0$	434.6	23 010	112	−1480
6s6p $^3P_2 \rightarrow 6s^2\ ^1S_0$[b]	498.0	20 080	...	370
$6p^2\ ^3P_1 \rightarrow$ 6s6p $^1P_1$[c]	529.7	18 880	180	140
6s6p $^3P_1 \rightarrow 6s^2\ ^1S_0$	545.9	18 320	250	330
6s6p $^3P_0 \rightarrow 6s^2\ ^1S_0$	561.9	17 800	490	510

[a]Peak characterized using LED emission spectrum.
[b]Signal-to-noise ratio is too small for a full characterization.
[c]Justification for this tentative assignment is given in Sec. V.

C. Excited state absorption spectra

As shown in Figure 4, absorption spectroscopy performed while the sample was being pumped into the triplet

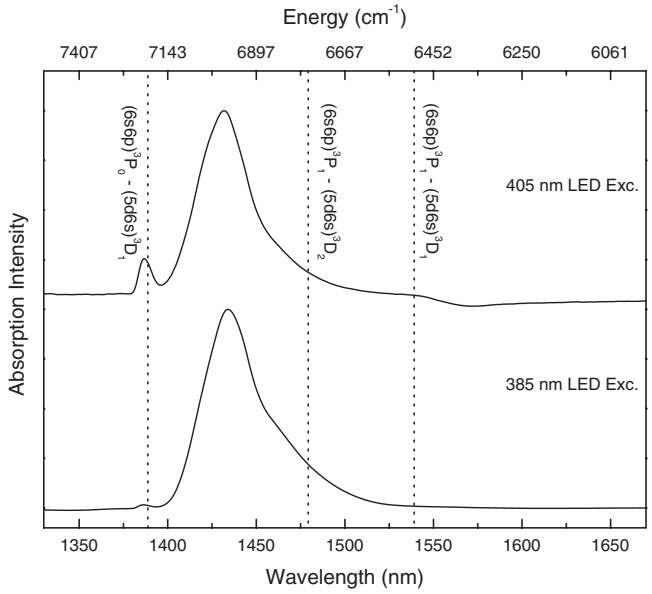

FIG. 4. Absorption spectra recorded while pumping with the 405 nm centered LED (top) and the 385 nm centered LED (bottom).

TABLE III. Principal features of the excited state absorption spectrum for the Yb/Ne system using the 405 nm centered LED. The symbols here are the same as those used in Table I. The uncertainty is assumed to be ± 2 cm^{-1} on all values.

Transition	λ (μm)	ν (cm^{-1})	Δ (cm^{-1})	δ (cm^{-1})
$6p^2\ ^3P_1 \rightarrow 5d6s\ ^3D_2$	1.43	6985	166	225
$6s6p\ ^3P_0 \rightarrow 5d6s\ ^3D_1$	1.39	7212	44	10

states reveals two main absorption features. Of the transitions arising from these states, the $6s6p\ ^3P_1 \rightarrow 5d6s\ ^3D_2$ transition has the largest electronic dipole amplitude[15] and so the large peak centered at 6985 cm^{-1} was assigned to it. The clear asymmetry of this peak due to a blue shoulder in the 1450−1550 nm region provides further evidence of Yb occupation in secondary trapping sites.

Based on its proximity and electronic dipole amplitude, the second peak centered at 7212 cm^{-1} was assigned to the $6s6p\ ^3P_0 \rightarrow 5d6s\ ^3D_1$ transition (see Table III). This peak was observed to be much more pronounced when pumping with the 405 nm centered LED than with the 385 nm centered LED, demonstrating the former to be more efficient in populating the metastable $^3P_0$ state.

IV. MODEL FOR THE POTENTIAL ENERGY SURFACES

A. Pairwise potential model

As the first step towards the characterization of the PESs relevant to Yb atoms isolated in RG matrices, we considered here a simple diabatic model based on the following assumptions:

(i) Many-body interactions are weak and can be neglected to represent the PES of the Yb · RG$_n$ cluster as the sum of pairwise interactions.
(ii) Interactions with RG atoms only weakly perturb the electronic structure of the isolated Yb atom and leave its electronic angular momenta unaltered.
(iii) Spin-orbit interaction in the Yb atom dominates over the interatomic interactions. The total angular momentum J together with its projection M onto the space-fixed (SF) axis Z and reflection parity σ for $M = 0$, provides the proper classification of the Yb · RG electronic states.
(iv) Mixing between the different M components of the J-manifold can be neglected within this approximation.

This model therefore treats J and M^σ as good quantum numbers, allowing for coupling in the case of curve crossings between states of different J and the same M^σ.

Placing the origin of the SF frame at the Yb nucleus, one can therefore express the PES of each J, M state as

$$W_{JM}(\mathbf{R}_1, \ldots \mathbf{R}_n) = \sum_{i=1}^{n} V_{JM}(\mathbf{R}_i) + \sum_{i=1}^{n} \sum_{j=1}^{i-1} U(|\mathbf{R}_i - \mathbf{R}_j|). \quad (1)$$

Here, $\mathbf{R}_i$ is the coordinate of ith RG atom and U is the isotropic potential of the RG · RG interaction. For each i, the Yb · RG potential V_{JM} is given by a linear combination of the diatomic potentials $V_{J\Omega}(R_i)$, where Ω is the projection of J onto the $\mathbf{R}_i$ radius-vector. Coefficients of this combination are defined by the rotation matrices connecting the diatomic $\mathbf{R}_i$ and SF frames and depend on the corresponding Euler angles ϕ_i and θ_i.

This model is practically equivalent to that exposed in detail by Beswick *et al.*[16,17] (see also Refs. 4 and 18), with two exceptions. First, according to assumption (iv), we used only the diagonal matrix elements $M' = M$ ($\Omega'_e = \Omega_e$ in Beswick's notation) to represent the PESs. Second, we made a straightforward extension to the $J = 2$ case.

B. *Ab initio* Yb · Ne potentials

The Ne · Ne potential U in Eq. (1) can be found in Ref. 19, whereas for Yb · RG dimers only the ground-state Yb · He potential is available in the literature.[20] We therefore performed an *ab initio* study of the Yb · Ne dimer using the MOLPRO program package.[21] The full set of the spin-orbit (SO) coupled potentials correlated to the lowest $^1S_0$, $^{1,3}P_J$, and $^{1,3}D_J$ limits of atomic Yb was obtained as described in the supplementary material.[22] The dimer states are classified within Hund's coupling case (c) as Ω^σ, with Ω being the projection of J onto R. The corresponding SO-coupled potentials are designated as $V_{J\Omega}$ with the meaning that J is an asymptotically good quantum number.

Figure 5 shows the SO-coupled potentials for the dimer states correlated to the lowest limits of atomic Yb. All of them possess very shallow wells indicating that electronic excitations maintain predominantly weak dispersion bonding. Furthermore, interactions in the degenerate $J \neq 0$ states are quite anisotropic, i.e., exhibit remarkable dependence on Ω. To simplify the modeling, we represented the SO-coupled

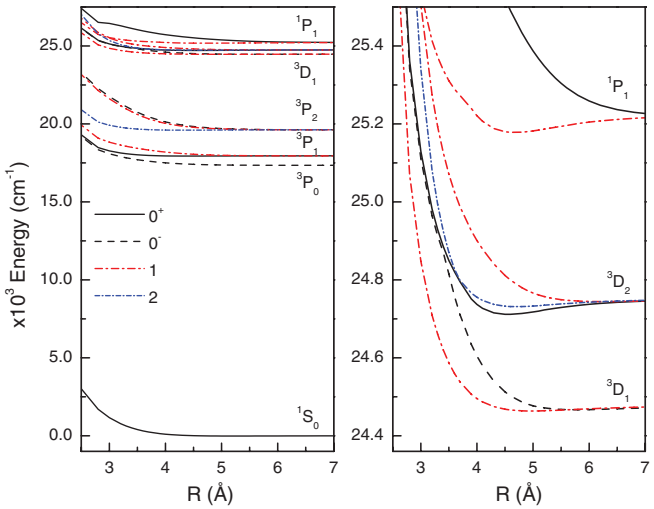

FIG. 5. *Ab initio* SO-coupled Ω^σ potentials of the Yb · Ne dimer. Left panel: an overview. Right panel: an enlarged view of the potentials correlated to closely lying $^3D_{1,2}$ and $^1P_1$ terms.

TABLE IV. Parameters of the Morse functions for the SO-coupled Yb · Ne potentials.

Ω^σ $^{2S+1}L_J$	D (cm^{-1})	R_e (Å)	α (Å^{-1})
$X0^+$ $^1S_0$	14.7	5.23	1.10
0^- $^3P_0$	4.7	6.28	0.86
0^+ $^3P_1$	17.5	4.43	1.32
1 $^3P_1$	4.5	6.53	0.85
0^- $^3P_2$	3.0	6.90	0.18
1 $^3P_2$	3.2	6.95	0.78
2 $^3P_2$	25.8	4.14	1.30
0^- $^3D_1$	11.4	5.78	0.86
1 $^3D_1$	14.7	4.99	0.93
0^+ $^3D_2$	40.5	4.55	1.12
1 $^3D_2$	7.3	6.22	1.07
2 $^3D_2$	20.3	4.70	1.06
0^- $^3D_3$	27.4	4.65	1.13
1 $^3D_3$	20.2	4.52	1.02
2 $^3D_3$	7.0	6.46	1.13
3 $^3D_3$	6.8	6.01	0.77
0^+ $^1P_1$	1.4	8.47	0.26
1 $^1P_1$	43.9	4.67	1.10
0^+ $^1D_2$	2.7	6.91	0.22
1 $^1D_2$	25.7	5.07	1.06
2 $^1D_2$	9.9	4.98	0.48

potentials by the Morse functions

$$V(R) = D[e^{-2\alpha(R-R_e)} - 2e^{-\alpha(R-R_e)}]$$

with the equilibrium distance, R_e, and dissociation energy, D, determined by the spline interpolation of the *ab initio* points and the range parameter, α, calculated using the harmonic vibrational frequency. Parameters obtained for the relevant potentials are listed in the Table IV.

C. Modeling of the Yb · Ne$_n$ cluster

M · RG$_{18}$ cluster models have most successfully simulated the emission and absorption features of matrix isolated species for the case in which the M · RG bond length is comparable to the RG · RG separation inside the matrix.[4,18] The metal atom is then assumed to occupy a single substitutional trapping site in a highly symmetric cluster for which the twelve nearest-neighbor RG atoms of the first solvation shell are separated from the M atom by $R_0 = a/\sqrt{2}$, while the six RG atoms of the second solvation shell are located at the $R_0 = a$ distance, where a is the lattice parameter.

In the present case, however, the large discrepancy between the Yb · Ne ground state bond length (5.23 Å) and the Ne lattice parameter (4.47 Å) makes occupation in an undistorted single substitutional site unlikely. A similar problem has been treated in the simulation of Cd/RG systems,[5] where the Cd · Ar ground state bond length (4.31 Å) is larger than the Ar substitutional site diameter (3.76 Å), and the Cd · Ne ground state bond length (4.26 Å) is larger than the Ne substitutional site diameter (3.15 Å). For the Cd/Ar system, the authors considered a cluster with a larger lattice parameter to represent a substitutional site expanded to accommodate the large Cd · Ar bond length. For the Cd/Ne system, occupation in a multivacancy trapping site was proposed.

To gain qualitative support to our observations, we considered here two expanded clusters that model the trapping sites obtained by single substitutional (ss) and multivacancy (mv) occupation in the fcc Ne lattice. In both cases, the axial separation of each C_4 group of Ne atoms from the Yb center was limited from above by the lattice parameter (otherwise, these Ne atoms formally leave the elementary fcc cell). For the ss site model, the twelve nearest-neighbor Ne atoms are then separated from the Yb atom by $R_0 = a\sqrt{2}$, while the six next nearest-neighbor Ne atoms are located at the $R_0 = 2a$ distance. As a simple approximation to mv occupation, we assumed that the Yb atom displaces an additional three Ne atoms (the total number of atoms displaced is then the same as in a tetravacancy). In this case, the calculation was repeated with a Yb · Ne$_{15}$ cluster after removing three atoms from a C_4 group of nearest-neighbors.

We calculated the PESs resulting from cluster deformations in the triply degenerate F_{1u} mode, i.e., for the displacement of the Yb atom, q, along the SF Z axis (labeled the "Q2 body mode" in Ref. 4). The SF Z axis itself was taken to be one of the C_4 axes of the octahedron formed by the Ne atoms in the first solvation shell, along which the p_Z orbital is also polarized. The X and Y axes were then chosen from the remaining two C_4 axes perpendicular to the SF Z axis (Figure 6). Insofar as this simplified potential model considers M as the good quantum number, we used M^σ notations for cluster states.

For an understanding of the spectral features associated with closely lying $^1P_1$ and ^3D_J terms, it is of prime importance to identify which states correlate to bound and unbound PESs. Figure 7 shows that in the vibrational mode considered here,

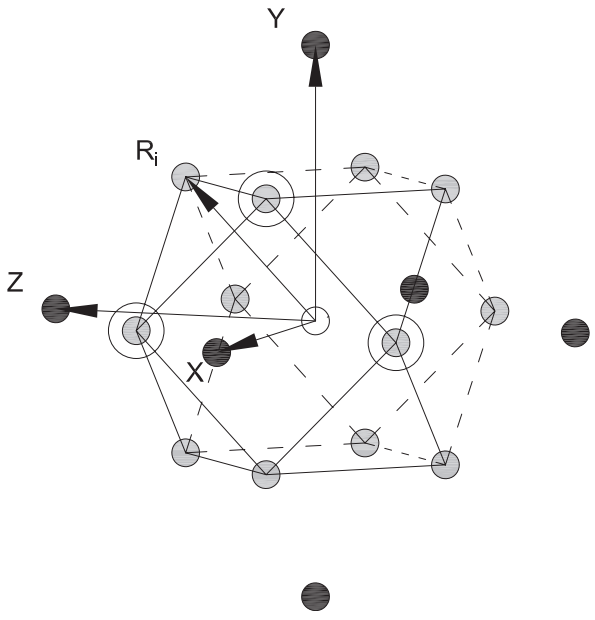

FIG. 6. Illustration of the Yb atom (white) at the center of a Yb · Ne$_{18}$ cluster. The twelve nearest-neighbor Ne atoms are shown in gray, while the six next nearest-neighbor Ne atoms are shown in black. The lines outlining each C_4 group of atoms are solid in the foreground and dashed in the background. The three Ne atoms displaced in the Yb · Ne$_{15}$ cluster model are shown circled.

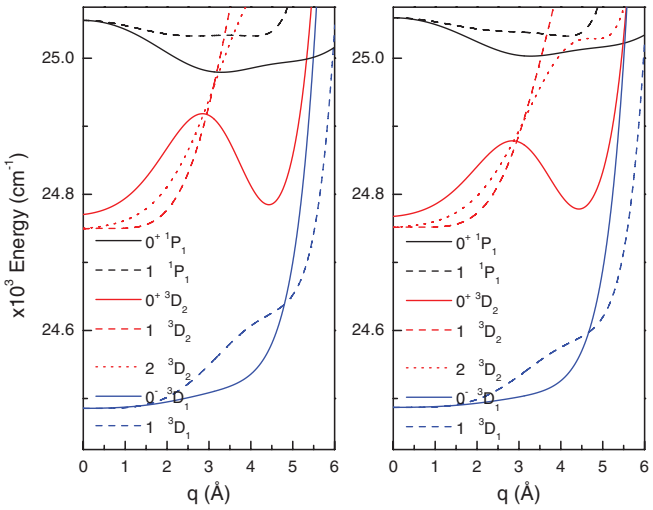

FIG. 7. Sections of the PESs generated by the cluster model for (i) occupation in a single substitutional site (left) and (ii) occupation in a multivacancy trapping site (right). The states correlated to the $^3D_1$, $^3D_2$, and $^1P_1$ terms are classified as M^σ.

for both ss and mv site models, the PES correlated to the 0^+ $^1P_1$ state is attractive, while that correlated to the 1 $^1P_1$ state (although weakly bound in some regions) has a generally repulsive character. This contrasts with the Yb · Ne diatomic case, for which, as shown in Figure 5 and Table IV, the PES correlated to the 1 $^1P_1$ state ($D = 43.9$ cm^{-1}) is much more strongly bound than that correlated to the 0^+ $^1P_1$ state ($D = 4.67$ cm^{-1}). It is nonetheless consistent with the typical behavior of the spin-singlet state in matrix isolation, as observed in the Zn/RG and Hg/RG systems.[4,6]

The second important insight provided by the cluster model regards the interaction between $^1P_1$ and $^3D_{1,2}$ states in isolation. As shown in Figure 7, for both ss and mv site models, the PESs correlated to the 0^+, 1, and 2 $^3D_2$ states intersect that of 0^+ $^1P_1$ state. The same is also true for the PESs correlated to the 0^- and 1 $^3D_1$ states. We broadly identify these curve crossings as the mechanism behind the enhanced ISC observed in the Yb/Ne system and discuss the most probable channel for it in Sec. V.

V. DISCUSSION

A. Matrix shifts and spectral assignments

The absorption spectra (Figure 2) show that the $6s^2$ $^1S_0 \rightarrow 4f^{13}5d^26s$ transition and the $6s^2$ $^1S_0 \rightarrow 6s6p$ $^1P_1$ transition are both blueshifted in Ne, the former by 190 cm^{-1} and the latter by 680 cm^{-1}. The cluster calculation of Sec. IV addresses a large amplitude vibrational mode to explain the emission process and may not accurately reproduce the small amplitude displacements around the ground state equilibrium configuration that simulate absorption. Nonetheless, a close examination of the various 0^+ and 1 $^1P_1$ contributions to the cluster PESs provides a clue to the results of the absorption spectra, predicting a blueshift for small Yb · Ne separations at which the strongly repulsive nearest-neighbor 0^+ interactions dominate over weakly attractive nearest- and next nearest-neighbor interactions.[23] This is in keeping with the expected predominance of short-range repulsive forces over long-range attractive ones in the case of cramped occupation in the lighter RGs as also cited for Zn/RG systems.[1]

Excitation into the center of the of the $6s^2$ $^1S_0 \rightarrow 6s6p$ $^1P_1$ absorption peak produced the emission spectra of Figure 3. A comparison of the position of its peaks with the gas phase frequencies of the low-lying levels of Yb was sufficient to make the assignments of Table II. An unusually large redshift was observed in the $5d6s$ $^3D_1 \rightarrow 6s^2$ $^1S_0$ transition (-1480 cm^{-1}), which we are currently unable to explain. We therefore look to a more accurate simulation of the trapping sites and measurements in other RGs to resolve this issue.

The emission spectra also revealed an unexpected peak at 530 nm. The $6s6p$ $^3P_2$ state decay was initially thought to be the source of this emission, however, a number of considerations make it unlikely. The first is that assignment to the $^3P_2$ state would imply a redshifted emission, at odds with the blueshifted $^3P_1$ and $^3P_0$ state emissions. The second is that the source of the 530 nm emission was found to have a lifetime lower than 25 ms. Although the matrix environment is expected to partly quench the metastability of the $^3P_2$ state, a reduction of the lifetime by three orders of magnitude from the gas phase 12.3 s value looks too severe. (For instance, the lifetime of the $^3P_0$ state in isolation was only reduced by a factor of approximately four.) The third is that no $6s6p$ $^3P_2 \rightarrow 5d6s$ $^3D_{1,2,3}$ transitions were observed in the absorption spectra of Yb in its excited states, despite their dipole amplitudes being comparable to those of the observed $6s6p$ $^3P_{1,2} \rightarrow 5d6s$ $^3D_{1,2}$ transitions.[15]

Discounting the $^3P_2$ state as the source of the 530 nm emission, we tentatively suggest that decay from a higher state is responsible following the absorption of a second photon. A good candidate is a decay to the $6s6p$ $^1P_1$ state from the much higher $6p^2$ $^3P_1$ state. Population of this state is proposed to occur simultaneously with the optical pumping of the singlet state. The $6s6p$ $^3P_1 \rightarrow 6p^2$ $^3P_1$ transition occurs at 387 nm in the gas phase and under matrix conditions is expected to be sufficiently broadened to be excitable by the laser frequency of 389 nm. The $6p^2$ $^3P_1$ state then has an allowed decay to the $6s6p$ $^1P_1$ state at a nearby frequency of 533 nm in the gas phase.

The $6p^2$ $^3P_1$ state is also accessible through the $6s6p$ $^3P_0 \rightarrow 6p^2$ $^1P_1$ transition at 374 nm in solid Ne.[12] Inadvertent population of this state would explain the difference in the relative amplitude of the $6s6p$ $^3P_0 \rightarrow 5d6s$ $^3D_1$ absorption observed with different LEDs. Initially, we expected optical pumping with the 385 nm LED to be more efficient due its proximity to the singlet state resonant transition of the Yb/Ne system. However, the large bandwidth of the 385 nm LED means that it had a significant component overlapping with the depopulating $6s6p$ $^3P_0 \rightarrow 6p^2$ $^1P_1$ transition. In contrast, the peak of the 405 nm LED excitation was sufficiently far away from the frequency of this transition to minimize depopulation.

A decisive test of the 530 nm assignment proposed here would require a lifetime measurement of the $^1P_1$ state following the shutdown of the optical pump. The presence of a rise time component in the decay curve of its emission would indicate that it is being fed from a higher state. Given the short

lifetime of the $^1P_1$ state (~5 ns), however, we do not presently have the temporal resolution to measure it and leave this issue for further investigation.

B. Excited state absorption spectra and intersystem crossing

In the absorption spectra of Yb in its excited states (Figure 4), we observed two peaks, one at 6985 cm^{-1} and the other at 7212 cm^{-1}. They were assigned, respectively, to the 6s6p $^3P_1 \rightarrow$ 5d6s $^3D_2$ and the 6s6p $^3P_0 \rightarrow$ 5d6s $^3D_1$ transitions. We explain these frequencies in relation to those observed in our absorption and emission spectra by applying the Frank-Condon principle within the context of a single configuration coordinate model. We also assume that at low temperature (4.2 K) Frank-Condon vertical transitions arise from the lowest vibrational-phonon level.

Figure 8 illustrates how the low-lying electronic structure of Yb isolated in Ne can be inferred from the three spectra. After excitation of the singlet transition, fast non-radiative decay to the lowest $v = 0$ phonon level of the strongly bound PES correlated to the 0^+ $^1P_1$ state occurs, followed by radiative decay to the ground state and non-radiative decay to the matrix isolated $^3D_{1,2}$ states. The $^3D_{1,2}$ states in turn couple radiatively with the ground state and the triplet manifold, specifically, the $^3D_1$ state with the $^3P_0$ state and the $^3D_2$ state with the $^3P_1$ state. From our cluster model, we have inferred that the dominant frequency component of decays from $^3D_2$ state originates from the bound region of the PES correlated to the 0^+ $^3D_2$ state. From our excited state absorption spectra, we expect that transitions from the ^3P_J state to the $^3D_{1,2}$ states couple above the $^1P_1$ ($q = 0$) PES asymptote, in which case there will be considerable overlap between the vibrational-phonon levels of the matrix isolated $^3D_{1,2}$ states and $^1P_1$ states.

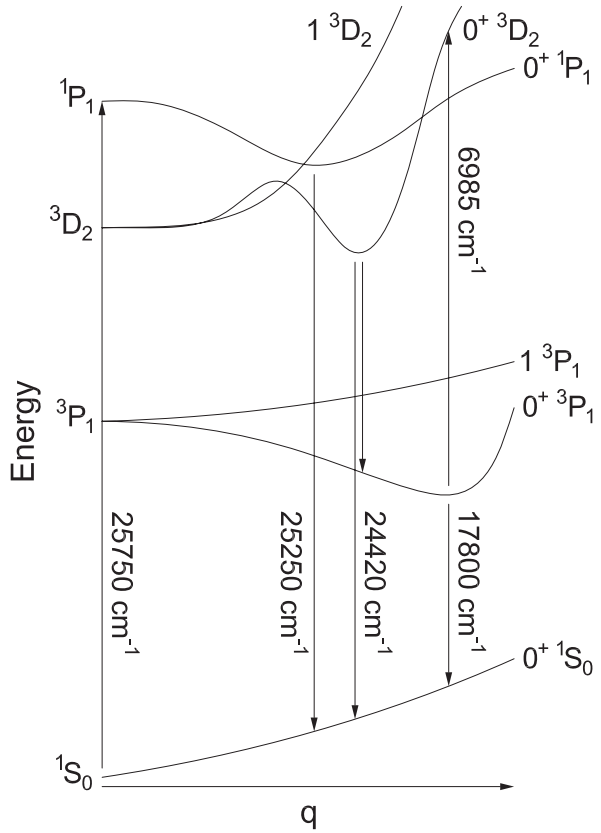

FIG. 8. Schematic configurational coordinate diagram showing the relative position of the PESs of the low-lying states of the Yb/Ne system as a function of the normal mode q. The atomic states to which they correlate are shown on the left-hand side. The Yb/Ne cluster states to which they correlate are shown in Hund's case (c) notation on the right-hand side. For clarity, transitions to and from the matrix isolated $^3D_1$ state have been omitted.

The proximity of the $^3D_{1,2}$ states PESs to that of the $^1P_1$ state plays an important role in the strong ISC observed for Yb isolated in Ne. The nearly complete quenching of the singlet emission in Figure 3 indicates that the ISC rate is comparable to the singlet decay rate (1.7×10^8 Hz) and a simple rate equation calculation based on this spectrum gives its value as 3.6×10^7 Hz. The branching ratio of the $^1P_1$ state to the $^3D_{1,2}$ states in isolation is therefore 0.17, several orders of magnitude larger than the gas phase value of 1.2×10^{-7}.[24]

Breckenridge *et al.* have successfully explained the ISC observed in Zn/RG systems in terms of the behavior of the strongly bound PES correlated to the $^1\Sigma$ 4p ^{1}P state (labelled in their work $^1A_1$) and that of the repulsive PES correlated to the $^3\Pi_1$ 4p ^{3}P state (labelled in their work ^3E).[4] The explanation is the same as that used in the analogous gas phase "half-collision" studies where interaction with a single RG atom may induce $Zn \cdot RG(^1\Pi_1)$ to $Zn \cdot RG(^3\Sigma_1)$ state ISC.[25] In both cases, ISC only occurs when there is an avoided curve crossing between the repulsive PES correlated to the M(*nsnp* ^3P_J) state and the attractive PES correlated to M(*nsnp* $^1P_1$) state with strong SO-induced mixing causing predissociation of the singlet state into triplet state products.

We adopt a similar rationale based on an interpretation of our cluster model and ascribe the high ISC rate of the Yb/Ne system to predissociation of the singlet state by surface hopping from the PES correlated to $^1P_1$ state to those of the $^3D_{1,2}$ states. In the models used for Zn/RG systems,[4] SO interaction between the non-relativistic states manifests itself in the avoided crossings that identify the possibility of surface hopping. Our model based on the SO-coupled states artificially gives the real crossings, but with the same implication. In Figure 7, the PESs correlated to the 0^+, 1, and 2 $^3D_2$ states and 0^- and 1 $^3D_1$ states all cross the 0^+ $^1P_1$ PES in both ss and mv site models. A calculation of the surface hopping probabilities for each predissocation channel would require a more thorough interaction model (i.e., built in the Hund's coupling case (a) basis with the proper rotational transformation of the non-diagonal SO matrix) that is beyond the scope of the present work. General considerations, however, indicate that the coupling between states of the same symmetry should be the most efficient, and we therefore identify the interaction between the 0^+ PESs correlated to the $^1P_1$ and $^3D_2$ states as the main cause of the high ISC rate observed here.

C. 6s6p $^3P_0$ and 5d6s $^3D_1$ decay

The 6s6p $^3P_0 \rightarrow$ 6s^2 $^1S_0$ and 5d6s $^3D_1 \rightarrow$ 6s^2 $^1S_0$ transitions that are ordinarily forbidden in the gas phase are found to be enhanced in isolation. The $^3P_0$ state, for instance, is

strongly metastable with no single photon decay mode to the ground state. This metastability is partially quenched in the odd isotopes (^{171}Yb and ^{173}Yb) by the hyperfine interaction giving the state in natural Yb a finite lifetime calculated to be 55.9 s.[14] The lifetime of this state was nonetheless measured at 14.5± 0.5 s, considerably shorter than its predicted value, which suggests there is an additional quenching mechanism present in isolation. As observed in Hg/RG systems,[26] emission from the metastable Hg(^{3}P$_0$) atom is possible if the symmetry of the emitting center is lowered. We therefore attribute the quenching of the ^{3}P$_0$ state to distortions introduced into the crystal structure in accommodating the large Yb · Ne ground state bond length.

In contrast to the parity forbidden 6s6p ^{3}P$_0$ → 6s^2 ^{1}S$_0$ transition, the metastable character of the 5d6s ^{3}D$_1$ state in the gas phase is dictated by spatial (angular momentum) selection rules. Interactions with RG atom(s) formally allow the transitions from these states to the ground ^{1}S$_0$ state through the dipole coupling of 1^+ to 0^+ components. In the case of the ^{3}D$_1$ state, this arises from second-order interaction with the P$_J$ states. The emission we observed from the ^{3}D$_1$ state is accordingly very weak.

VI. CONCLUSIONS

We have characterized the low-lying electronic states of Yb isolated in solid Ne through absorption and emission spectroscopy, as well as the absorption spectroscopy of Yb in its excited states. We found that the relative positions of the ^{3}P$_{0,1,2}$ and ^{3}D$_{1,2}$ states are qualitatively the same in isolation as in the gas phase, but that their photophysical characteristics are considerably altered. Combining the three spectra and supplementing them with a simple *ab initio*-based cluster model, we arrived at a qualitatively consistent picture of observed radiative and assumed non-radiative processes.

Obvious extensions of this work—experiments on Yb isolated in the heavier RGs and improvement of the theoretical model—are currently being explored. They should provide a deeper understanding of the complex photophysical processes in the matrix isolated Yb atom and its analogs.

ACKNOWLEDGMENTS

The authors thank Professor A. S. C. Cheung for the loan of a cw frequency doubler. They also thank Professor C. Crépin for useful discussions and the referees for their constructive comments, all of which were considered in preparing the final version of this paper. This work has been jointly supported by the NSFC (11150110457), the NKBRSF (2010CB923300), and the FRFCU. R. Lambo gratefully acknowledges support from the Chinese Academy of Sciences.

[1] V. A. Bracken, P. Gürtler, and J. G. McCaffrey, J. Chem. Phys. **107**, 5290 (1997).
[2] B. Healy and J. G. McCaffrey, J. Chem. Phys. **110**, 3903 (1999).
[3] C. Crépin and A. Tramer, J. Chem. Phys. **97**, 4772 (1992).
[4] W. H. Breckenridge, M. D. Morse, and J. G. McCaffrey, J. Chem. Phys. **109**, 3137 (1998).
[5] B. Healy and J. G. McCaffrey, J. Phys. Chem. A **104**(16), 3553 (2000).
[6] M. A. Collier and J. G. McCaffrey, J. Chem. Phys. **119**, 11888 (2003).
[7] O. Byrne and J. G. McCaffrey, J. Chem. Phys. **134**, 124501 (2011).
[8] O. Byrne, "Spectroscopy and photochemistry of europium atoms in low temperature solids— An experimental and theoretical study," Ph.D. dissertation, National University of Ireland, 2010.
[9] W. E. Klotzbucher, M. A. Petrukhina, and G. B. Sergeev, J. Phys. Chem. A **101**(25), 4548 (1997).
[10] S. Suzer and L. Andrews, J. Chem. Phys. **89**, 5514 (1988).
[11] M. J. Pellin, D. M. Gruen, T. Fisher, and T. Foosnaes, J. Chem. Phys. **79**, 5871 (1983).
[12] C.-Y. Xu, S.-M. Hu, J. Singh, K. Bailey, Z.-T. Lu, P. Mueller, T. P. O'Connor, and U. Welp, Phys. Rev. Lett. **107**, 093001 (2011).
[13] S.-M. Hu, L. Wan, J.-H. Du, G. Xu, W.-P. Deng, L. Wu, S.-X. Tian, and Y. Chen, Vib. Spectrosc. **50**, 36 (2009).
[14] A. P. Mishra and T. K. Balasubramanian, J. Quant. Spectrosc. Radiat. Transf. **69**, 769 (2001).
[15] S. G. Porsev, Y. G. Rakhlina, and M. G. Kozlov, Phys. Rev. A **60**, 2781 (1999).
[16] A. Bastida, J. Zúñiga, A. Requena, N. Halberstadt, and J. A. Beswick, Faraday Discuss. **97**, 131 (1994).
[17] J. Zúñiga, A. Bastida, A. Requena, N. Halberstadt, and J. A. Beswick, J. Chem. Phys. **98**, 1007 (1993).
[18] J. G. Kaup and W. H. Breckenridge, J. Phys. Chem. **99**, 13701 (1995).
[19] J. Koperski, *Van der Waals Complexes in Supersonic Beams* (Wiley-VCH, Weinheim, 2003).
[20] A. A. Buchachenko, G. Chałasiński, and M. M. Szczęśniak, Eur. Phys. J. D **45**, 147 (2007).
[21] H.-J. Werner, P. J. Knowles, F. R. Manby, M. Schütz *et al.*, MOLPRO, version 2010.1, a package of *ab initio* programs, 2010, see http://www.molpro.net.
[22] See supplementary material at http://dx.doi.org/10.1063/1.4768419 for full details of Yb · Ne *ab initio* calculations.
[23] Since the pair-potentials of the 4f^{13}5d^{2}6s state have not been calculated, we cannot comment on any matrix-induced effects on its absorption peak.
[24] K. Honda, Y. Takasu, T. Kuwamoto, M. Fujimoto, and K. Toyoda, Phys. Rev. A **59**(2), R934 (1999).
[25] S. Bililign, J. G. Kaup, and W. H. Breckenridge, J. Phys. Chem. **99**, 7878 (1995).
[26] C. Crépin, M. Chergui, T. Herbert, L. Koenig, P. Martin, and A. Tramer, J. Phys. Chem. **98**(13), 3280 (1994).